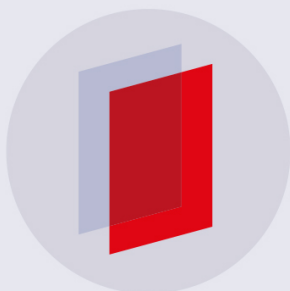


PAPER • OPEN ACCESS

Efficiency of cavity-enhanced high harmonic generation with geometric output coupling

To cite this article: M Högner *et al* 2019 *J. Phys. B: At. Mol. Opt. Phys.* **52** 075401

View the [article online](#) for updates and enhancements.



IOP | ebooks™

Bringing you innovative digital publishing with leading voices to create your essential collection of books in STEM research.

Start exploring the [collection](#) - download the first chapter of every title for free.

Efficiency of cavity-enhanced high harmonic generation with geometric output coupling

M Högner^{1,2} , T Saule^{1,2} and I Pupeza^{1,2,3} 

¹Max-Planck-Institut für Quantenoptik, Hans-Kopfermann-Straße 1, D-85748 Garching, Germany

²Ludwig-Maximilians-Universität München, Am Coulombwall 1, D-85748 Garching, Germany

E-mail: mhoegner@mpq.mpg.de and ioachim.pupeza@mpq.mpg.de

Received 29 January 2019

Accepted for publication 13 February 2019

Published 12 March 2019



CrossMark

Abstract

Cavity-enhanced high-order harmonic generation (HHG) affords broadband, coherent extreme-ultraviolet (XUV) pulse trains with repetition rates of several tens of MHz. Geometrically coupling out the intracavity generated XUV beam through a small on-axis hole in the cavity mirror following the HHG focus has enabled scaling the photon energies attainable with this technology to 100 eV and more, promising new applications of XUV frequency-comb spectroscopy and attosecond-temporal-resolution, multidimensional photoelectron spectroscopy and nanoscopy. So far, in this approach the features of the macroscopic response of the gas target are neither accessible directly nor indirectly via the out-coupled XUV beam due to the loss of spatial information caused by the truncation at the hole. Here, we derive a simple analytical model for the divergence of the intracavity harmonic beam as a function of experimental design parameters such as gas target position, cavity geometry and driving pulse intensity, thereby establishing a connection between the measured XUV spectra and the macroscopic response of the intracavity nonlinear medium. We verify this model by comparison to numerical simulations as well as to systematic measurements, and apply it to elucidate a trade-off between the efficiency of geometric output coupling and that of the HHG process, and the underlying physical mechanisms. These findings illuminate the share of the output coupling efficiency to the overall HHG conversion efficiency and provide—together with previously studied plasma-related enhancement limitations—a holistic means of optimizing the overall efficiency with this architecture that uniquely combines high repetition rates with high photon energies. Furthermore, quantitatively connecting the output coupled, observable XUV radiation to the nonlinear conversion at the cavity focus allows for a better insight into the dynamics of intracavity HHG and might benefit other applications of femtosecond enhancement cavities, such as high-repetition-rate HHG spectroscopy.

Keywords: high harmonic generation, enhancement cavity, conversion efficiency, geometric output coupling

(Some figures may appear in colour only in the online journal)

1. Introduction

Since its discovery in the late 80s [1, 2], laser-driven high-order harmonic generation (HHG) in gases has become an

indispensable source of coherent, table-top extreme-ultraviolet (XUV) radiation for the study of femtosecond and attosecond time-scale electron dynamics in atoms, solids and molecules [3, 4]. In modern HHG systems, the nonlinear conversion is driven by amplified femtosecond pulses, reaching energies of several 100 μJ [5–9]. Typically, this results in repetition rates significantly lower than 1 MHz. However, some applications require operation in the multi-10 MHz repetition-rate regime. Examples include experiments involving the detection of charged particles such as photoelectron spectroscopy and microscopy [10–12] and coincidence measurements [7],

³ Author to whom any correspondence should be addressed.



Original content from this work may be used under the terms of the [Creative Commons Attribution 3.0 licence](https://creativecommons.org/licenses/by/3.0/). Any further distribution of this work must maintain attribution to the author(s) and the title of the work, journal citation and DOI.

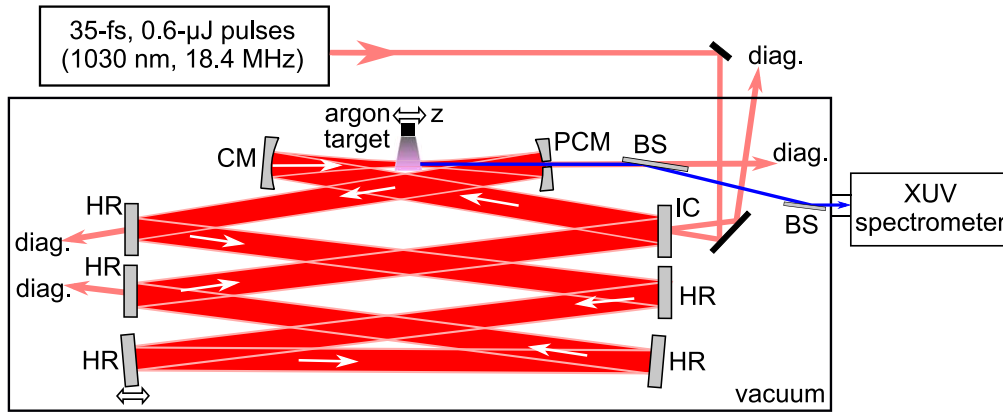


Figure 1. Setup for acquiring systematic p - z -maps of circulating power and XUV photon counts per harmonic order [19]. p : pressure, z : longitudinal target position relative to the focal plane, HR: highly reflective mirror, CM: curved HR mirror, PCM: pierced curved HR mirror, IC: input coupler, BS: XUV/IR beam splitter, diag.: diagnostics.

where space-charge effects limit the useful number of particles per pulse, and frequency-comb spectroscopy [13, 14] at high photon energies, where the power per comb line scales with the repetition rate and the comb spacing should be larger than the line width of the studied transition.

To date, femtosecond enhancement cavities (EC) constitute the most successful HHG approach combining high repetition rates with high XUV powers and high photon energies [15–17]. In cavity-enhanced HHG, the pulses passing the gas target are recycled with the help of a passive resonator housing the gas target (see figure 1). In doing so, inside of the EC a circulating pulse with an energy comparable to that of kHz HHG systems is obtained, without the necessity of reducing the repetition frequency of the original multi-MHz femtosecond front-end. Typically, in cavity-enhanced HHG, the pulse energy of the impinging laser is enhanced by around two orders of magnitude [15–19]. Coupling out the generated XUV radiation through a small on-axis opening in the mirror following the HHG focus [15, 20–22] has rendered the photon energies attainable with this technology scalable to 100 eV and more [15, 16].

While in state-of-the-art ECs circulating pulses of just a few tens of femtoseconds with multi-kW average powers have been demonstrated [16, 17], the overall conversion efficiencies (impinging power to out-coupled XUV power) of these systems have so far remained below the ones achieved with single-pass systems (see appendix A). This indicates that the constraints set by the resonator entail inefficiencies in the XUV generation and output coupling processes that counteract the significant enhancement of the impinging power. To reach the full potential of EC-based XUV sources, it is crucial to understand the individual contributions to these inefficiencies and investigate ways of mitigating them. Indeed, during the last years, considerable progress has been made in this direction. One such limitation is the phenomenon of intracavity intensity clamping, where plasma formation in the gas target on the time scale of a single pulse shifts the spectrum to shorter wavelengths and gives rise to a spectral phase, reducing the spectral overlap with the impinging pulse train and severely limiting the achievable XUV power [23, 24]. Furthermore, for high repetition rates, the generated

plasma embedded in the target gas stream can neither clear the interaction region nor decay before the arrival of the subsequent pulse, leading to the formation of a cumulative plasma. Recently, this has been shown to strongly impair the conversion efficiency [18, 19]. Decreasing the finesse of the resonator and increasing the gas velocity [18] or choosing a sufficiently low repetition rate [17, 19] constitute strategies of mitigating these effects, so that overall conversion efficiencies approaching that of single-pass systems were achieved [17].

In this work, we study the trade-off between intracavity XUV generation efficiency and geometric output coupling efficiency, which is governed by the position of the gas target relative to the focal plane. To this end, we developed a numerical model permitting to break down the overall conversion efficiency into its individual contributions, in particular the output coupling efficiency. We validate this model by finding excellent agreement with systematic measurements in a state-of-the-art cavity-enhanced HHG experiment, where the relevant parameters for output coupling and phase matching (backing pressure and gas target position) were scanned. Finally, we provide a physical explanation for the observed dependence of the output coupling efficiency on the target position and derive a simple approximation formula for the intracavity harmonic beam divergence.

These findings allow for relating the out-coupled XUV spectrum to the spatial and spectral shape of the XUV generated in the EC and, therefore, are crucial to understanding the intracavity HHG dynamics. In particular, alongside the mentioned insights concerning the plasma-related effects, they provide the missing piece for a complete picture of conversion efficiency contributions in photon-energy-scalable cavity-enhanced HHG.

2. Methods

2.1. Experimental data

The experimental setup for the acquisition of the parameter scans of XUV photon counts and driving average power is

described in detail in [19]. In short, a high-finesse 8-mirror resonator (see figure 1) with symmetric focusing (focal length 100 mm), operated near the inner stability edge and with an input coupler transmission of 3% was used to enhance 18.4 MHz, 35 fs, 0.6 μJ pulses spectrally centered at 1030 nm. XUV was generated in an argon gas target ejected from a 100 μm diameter-opening-nozzle placed near the 12.3 μm focus ($1/e^2$ -intensity radius, measured by imaging the mode on the output coupling mirror). XUV radiation was geometrically output-coupled through a 150 μm diameter circular opening in the cavity mirror following the HHG focus. The driving intracavity pulses were characterized with an optical spectrum analyzer and an autocorrelator, yielding pulse durations of 38 fs. A full scan of the gas target position z relative to the focal plane ($z > 0$ signifies that the gas target is placed behind the laser focus) and the backing pressure p applied to the nozzle was performed and the circulating infrared (IR) power and, using an XUV spectrometer, the output-coupled XUV photon counts per harmonic order were recorded at each point, resulting in the p - z -maps shown in figure 2(a).

2.2. Computational model

Assuming a 35 fs Gaussian pulse spectrally centered at 1030 nm and a Gaussian beam with a beam waist of 12.3 μm as the driving field, for each value of p and z we compute the harmonic field in a transverse plane following the gas target. For this, we numerically solve the first-order propagation equation for the IR and XUV with the 3D HHG model described in [25], without employing envelope approximations. We assume rotational symmetry to speed up the computation, and use the ionization-induced current derived in [26] and the strong-field approximation [27] as source terms. The computational model accounts for plasma-induced lensing, absorption and spectral blue-shift, as well as for Kerr focusing and self-phase modulation. The peak power was chosen proportional to the measured intracavity power (figure 2(a) of [19]), with a maximum of 0.36 GW for best agreement between simulations and experiment. The gas velocities and densities at the nozzle exit and at the interaction site were computed with the analytical model described in [28, p 17ff], presuming a reservoir temperature of 300 K and a 100 μm nozzle placed at a distance of 120 μm from the beam axis for best agreement with the experimental data. We assume flat-top density profiles at both positions and choose its diameter at the interaction site (176 μm) so that the resulting gas flux agrees with the one at the nozzle exit. Propagation from the plane after the gas target to the pierced mirror was done with a Fresnel two-step propagator [29]. The out-coupled XUV power was then computed by spatially integrating over a circular aperture, and spectrally integrating over each harmonic order.

3. Results

The simulated out-coupled XUV power per harmonic order, in dependence of p and z , is depicted in figure 2(b). The

simulations reproduce well the main features observed in the experimental data (figure 2(a)).

To separate the XUV generation efficiency from the output coupling efficiency, we computed the XUV power before the output coupling mirror (figure 2(c)). Thus, the output coupling efficiency can be obtained by dividing the out-coupled power by the generated power (figure 2(d)).

To examine the impact of XUV reabsorption in the gas target, we repeated the simulation with a purely real XUV refractive index, effectively disabling reabsorption (figure 2(e)). Figure 2(f) shows the ratio of the generated XUV power with and without reabsorption. By comparing figures 2(c) and (e), one can see that reabsorption does not affect the qualitative shape of the p - z -maps for harmonic orders > 21 . We repeated the same simulation, but this time discarding the spectral phase of the XUV dipole response and neglecting refractive index in the XUV (figure 2(g)). This leads to perfectly constructive macroscopic interference, i.e. phase matching is enforced, so that the macroscopic response essentially only depends on the number of emitters and the microscopic efficiency. This allows us to isolate the effect of phase matching by dividing the generated XUV power (without reabsorption) by the one with enforced phase matching (figure 2(h)).

The p - z -maps depicted in figures 2(a)–(c), (e) and (g) were normalized to the maximum XUV power per harmonic order for better visibility. For a comparison of the maximum power per harmonic order in simulation and experiment, see figure 3(a).

4. Discussion

4.1. Agreement with the experiment

The experimental maps of the XUV photon counts (figure 2(a)) exhibit some distinctive features:

- (i) harmonic orders around the 33rd reach optimum power for target positions well before the focus, while the optimum position for higher and lower harmonic orders is close to the focus;
- (ii) the optimum pressure increases with increasing harmonic order;
- (iii) for higher harmonic orders, the maps exhibit a V-shaped structure, consisting of two regions with high power, one before the focus and one around the focus;
- (iv) figure 3(a) reveals that the highest power is achieved around the 31st harmonic, and the power drops to zero towards the harmonic orders 21st and 43rd.

All these features are clearly reproduced in the simulated maps (figure 2(b)), thus verifying the model and allowing us to use it to investigate the origins of these features and disentangle the contributing factors.

4.2. Explanation of the observed features

Feature (i) can be attributed partly to the output coupling efficiency (figure 2(d)) and partly to the microscopic

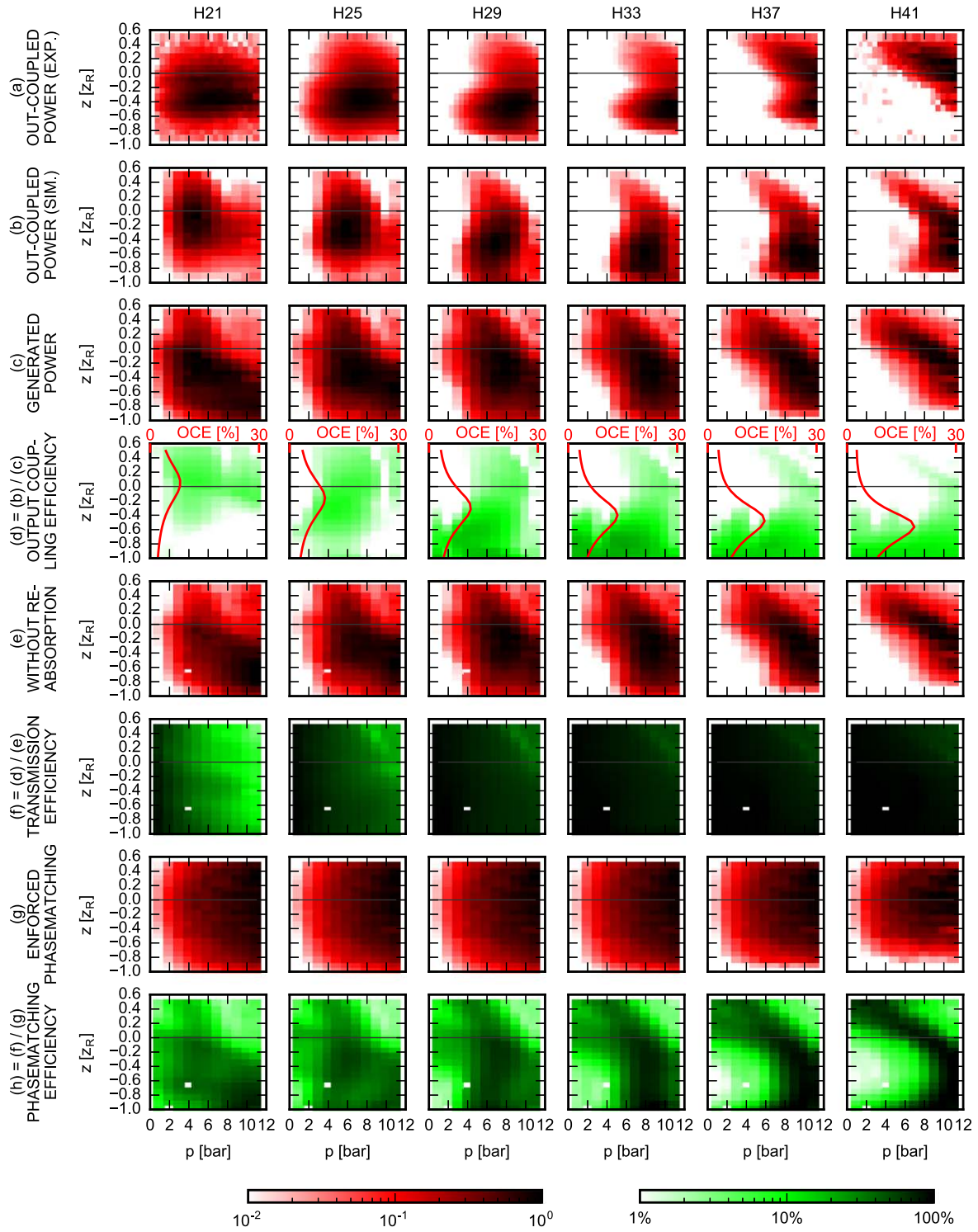


Figure 2. (a) Measured out-coupled XUV power for selected harmonic orders, taken from [19]. (b)–(h) Simulations. (b) Out-coupled XUV power. (c) Generated XUV power. (d) Output coupling efficiency, computed as the ratio between out-coupled and generated XUV power (color scale) and using the analytical formula (red line). (e) Generated XUV power without reabsorption. (f) Transmission efficiency, computed as the ratio between generated XUV power with and without reabsorption. (g) Generated XUV power with enforced phase matching and without reabsorption. (h) Phase matching efficiency, computed as the ratio of generated XUV power without and with enforced phase matching, both without reabsorption. (a), (b), (c), (e) and (g) are normalized for each harmonic order.

efficiency: for lower to intermediate harmonic orders, the optimum target position is dominated by the optimum output coupling efficiency, which is located close to the focal plane for lower orders, but significantly before the focal plane for

intermediate and higher harmonic orders (see section 4.4). For higher harmonic orders, however, the microscopic efficiency declines rapidly with increasing distance from the focus due to the high-harmonic cutoff (compare figure 2(g)).

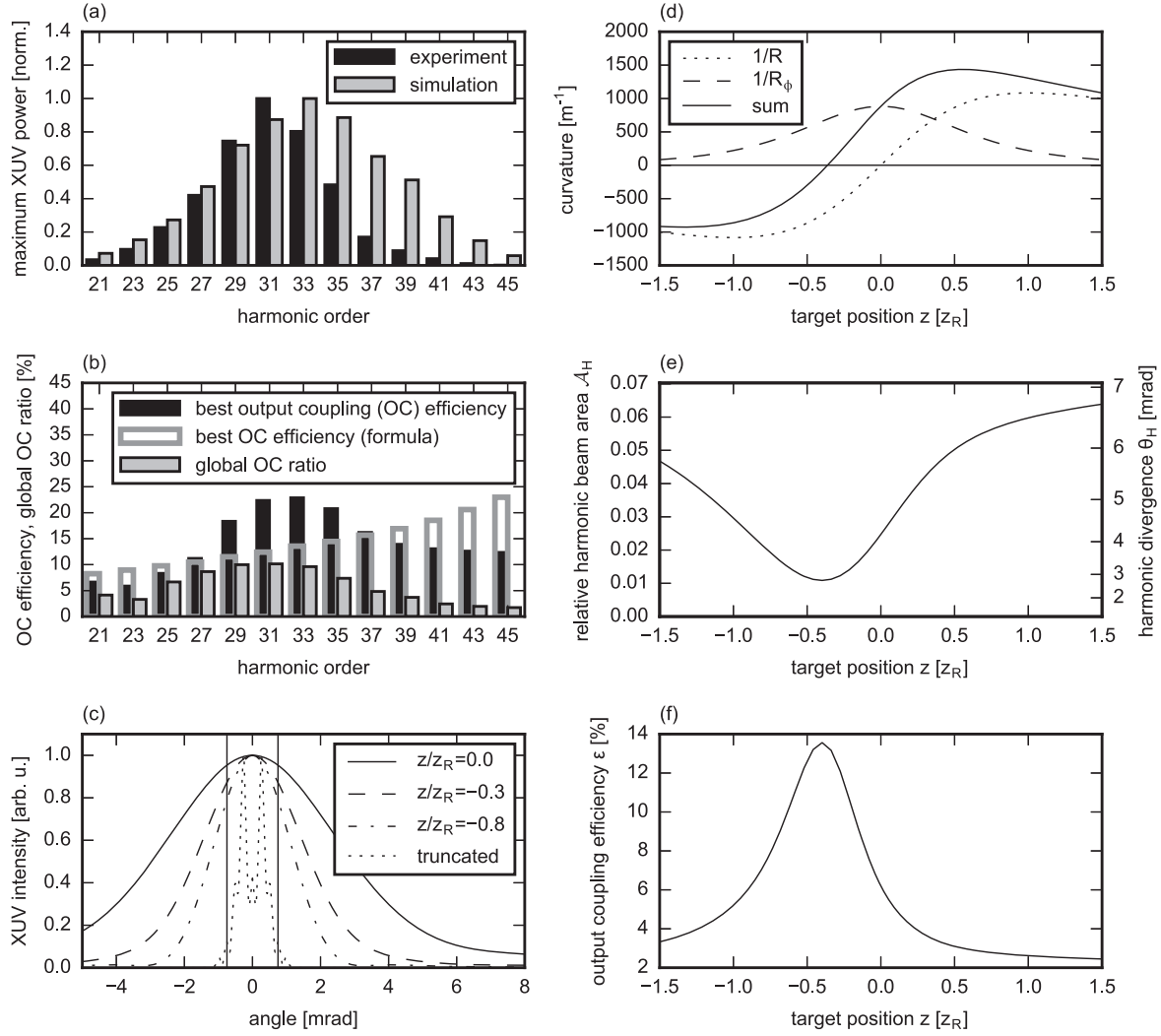


Figure 3. (a) XUV photon counts for each harmonic order at optimum target position and backing pressure, for experiment [19] and simulation, both normalized. (b) Optimum output coupling efficiencies for each harmonic as predicted by the numerical model (black) and the analytical model (gray edge), in comparison with the global output coupling ratio (optimum generated power to optimum out-coupled power from the numerical model, gray). (c) Simulated XUV beam profiles on the output coupling mirror for the 33rd harmonic generated at different gas target positions with a backing pressure of 8 bar. The vertical lines mark the hole diameter for 150 μm hole placed 100 mm after the gas target, and the dotted line shows the beam profile far behind the truncating hole mirror for a gas target positioned $0.56z_R$ before the focus, where z_R is the Rayleigh range of the driving beam. (d) Composition of the harmonic beam wave-front curvature $1/R_H = 1/R + 1/R_\phi$ (solid line) according to the analytical model for the 33rd harmonic, where $1/R$ (dotted) is the curvature of the driving beam and $1/R_\phi$ (dashed) is the additional curvature caused by the transverse dependence of the intensity-dependent harmonic dipole phase. (e) The resulting relative harmonic beam area $\mathcal{A}_H = \theta_H^2/\theta^2$, where θ_H is the divergence of the harmonic beam and θ the divergence of the driving beam. (f) The computed output coupling efficiency for a 150 μm hole placed 100 mm after the gas target.

The connection between harmonic order and optimum pressure (ii) can be explained by phase-matching (figure 2(h)): The contribution to the phase mismatch from the intensity-dependent dipole phase increases with harmonic order [30] and must be compensated for by increasing the contribution from the linear refractive index of neutral argon atoms, i.e. by increasing the density.

The V-shaped structure at high harmonic orders (iii) can be attributed to a combination of phase matching and output coupling efficiency: while the phase-matching maps exhibit the same structure (figure 2(h)), the lower wing is barely present in the maps of the generated XUV power and emerges

due to the high output coupling efficiency before the focus (figures 2(c), (d)).

The trend in figure 3(b) (feature (iv)) can be explained by considering the intertwining of output-coupling efficiency, the phase-matching efficiency and the number of emitters: For lower harmonic orders, the regions of high generation efficiency and high output coupling efficiency coincide (figures 2(c), (d)). The phase-matching pressure increases with harmonic order (ii), leading to a higher number of emitters and therefore higher XUV power (figure 2(g)). Additionally, the output coupling efficiency increases slightly with harmonic order. This explains the increase of the out-

coupled signal from lower orders towards the 31st harmonic. The decline for higher harmonic orders can be attributed to the fact that the regions of good generation efficiency and good output coupling do not coincide (see section 4.3), and that the phase-matching pressure was outside of the scanned pressure interval for harmonic orders >41 .

4.3. Trade-off between output coupling efficiency and generation efficiency

To determine how strongly the output coupling affects the achievable power, we compute the ratio between maximum out-coupled power and maximum produced power within the scanned p/z range for each harmonic, i.e. the ratio of the per-harmonic maxima of figures 2(b) and (c). It can be seen that for harmonic orders >35 only 2%–5% of the achievable XUV power in the cavity are accessible after output-coupling (figure 3(b), gray). In contrast, the optimum OCE, i.e. the highest OCE reached within the scanned p/z range, reaches up to 7 times higher values (figure 3(b), black). Consequently, optimum OCE is not reached at the same p/z values as optimum generated power.

As noted above, optimum output coupling efficiency is reached far before the focus (figure 2(d)). On the other hand, for higher harmonic orders, the optimum generation efficiency is reached for target positions around the focus (figure 2(c)). Hence, the optimum out-coupled XUV power is a result of a trade-off between generation efficiency and output-coupling efficiency, determined by the position of the gas target. For the parameters used here, geometric output coupling reduces the XUV power attainable outside the cavity by one to two orders of magnitude compared to the optimum power generated inside the cavity and therefore constitutes an important contribution to the overall conversion efficiency.

4.4. Physical background

4.4.1. Output coupling efficiency. As observed above, the output coupling efficiency depends on the gas target position, and target positions before the focus are beneficial for harmonic orders ≥ 29 . This can be attributed to a decrease of the harmonic beam divergence at these positions, as can be seen in figure 3(c), where the beam profiles on the output coupling mirror for different target positions are compared for the 33rd harmonic at a backing pressure of 8 bar.

To understand the physical reason for this behavior, we derive a simple analytical formula for the divergence of the harmonic beam. To this end, we assume a simple power law for the intensity dependence of the single-atom dipole response and a linear intensity-dependent phase, and approximate the harmonic beam as a Gaussian beam (see appendix C):

$$\mathcal{A}_H = \frac{1}{N_H} \frac{(\hat{z}^3 + \hat{z} + 2\gamma)^2 + (1 + \hat{z}^2)^2 \delta}{(1 + \hat{z}^2)^3}. \quad (1)$$

Here, \mathcal{A}_H is the harmonic beam area relative to the driving beam area on the output coupling mirror, $\hat{z} = z/z_R$ is

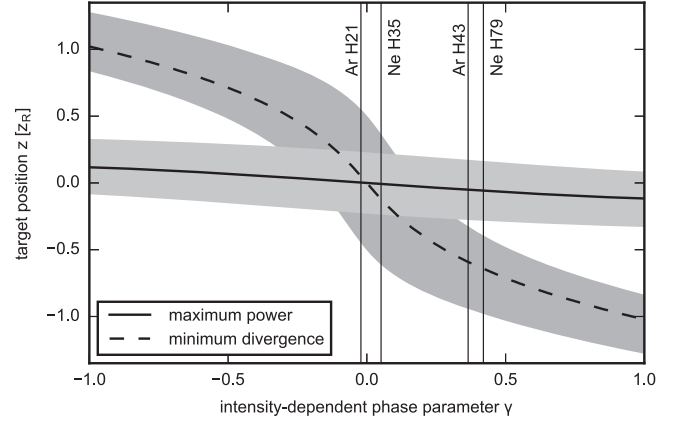


Figure 4. Optimum target position for generated XUV power (solid line) and output coupling (dashed line) versus the intensity-dependent phase parameter γ . The corridors mark the regions over which the power and the harmonic beam area deviate by less than a factor of 2 from the optimum values.

the scaled gas target position with the Rayleigh range z_R , and N_H , δ and γ are parameters describing the driving-intensity dependence of the single-atom dipole amplitude (N_H , $\delta = N_H^2/H^2$) and phase (γ) for a harmonic order H (see appendix B). The parameter $\gamma = \alpha_H I_f/H$ is referred to as *intensity-dependent phase parameter* in the following and depends on the intensity-dependent dipole phase gradient α_H and the intensity I_f in the focus.

Then, the output coupling efficiency can be written as

$$\epsilon = 1 - \exp(-2\mathcal{A}_o/\mathcal{A}_H), \quad (2)$$

where \mathcal{A}_o is the hole area relative to the driving beam area on the output coupling mirror. Figure 3(b) shows the agreement between the output coupling efficiency computed with this analytical formula and the values obtained from the simulations.

In good approximation, the relative harmonic beam area \mathcal{A}_H reaches its minimum (and thus, the output coupling efficiency ϵ its optimum) for gas target positions \hat{z}_{OC} where wave-front curvature $1/R_H$ of the harmonic beam in the plane of the gas target vanishes. This curvature comprises a contribution from the driving beam curvature $1/R$ and a contribution $1/R_\phi$ from the transverse harmonic phase that arises from the radially dependent driving field intensity (for details, see appendix C). In an intuitive picture, optimum output coupling efficiency is thus reached when the intensity-dependent harmonic phase balances out the wave-front curvature of the driving beam.

In figure 4, we show both contributions for the 33rd harmonic. As can be seen, the curvature $1/R_\phi$ due to the intensity-dependent harmonic phase is always positive for this harmonic order. Therefore, a vanishing total curvature $1/R_H$ is only possible at target positions before the focus, where the curvature $1/R$ of the driving beam is negative. Figures 3(e) and (f) show the resulting relative harmonic beam area and output coupling efficiency, respectively. This explains the decrease of the harmonic divergence for target positions before the focus, as observed in the simulated data (figure 3(c)).

4.4.2. Generated XUV power. With the same assumptions on the intensity-dependence of the single-atom dipole response and neglecting reabsorption as well as the Kerr and plasma contributions, we can also derive an analytical formula for the dependence of the generated XUV power on the gas target position. To this end, the phase matching pressure is calculated from the linear phase mismatch, the Gouy phase and the intensity-dependent dipole phase. Then, the harmonic power is estimated by considering the number of emitters and the dependence on the driving field intensity (see appendix D). For the parameters of the experiment, this formula predicts that optimum XUV power is generated for target positions very close to the focus ($|z/z_R| < 0.2$). For comparison, the numerical simulations predict optimum XUV power around $z/z_R = -0.25$ for all harmonics (see figure 2(c)).

4.4.3. Trade-off. The target position \hat{z}_{OC} for optimum output coupling as well as the position \hat{z}_{gen} for the optimum generated XUV power are functions of the parameters N_H , δ and γ . However, their dependence on N_H and δ is weak and can be neglected (see appendices C and D). Both optimum positions versus the intensity-dependent phase parameter γ are depicted in figure 4, alongside with corridors showing the \hat{z} ranges where the relative harmonic beam area doubles and the generated XUV power drops two half of the maximum, respectively. It becomes apparent that a trade-off detrimental for the accessible XUV power must be expected when the value of the intensity-dependent phase parameter deviates too much from zero.

Vertical lines in figure 4 mark the γ parameters for generation of harmonics in argon at a peak intensity of $1.5 \times 10^{14} \text{ W cm}^{-2}$ in the focus and in neon at $3 \times 10^{14} \text{ W cm}^{-2}$, for a driving wavelength of 1030 nm. As observed in the simulations for argon, the trade-off manifests itself mainly for higher harmonic orders. Figure 4 confirms that this finding can be generalized to HHG in neon.

4.4.4. Optimum output coupling efficiency. To compute the minimum harmonic beam area from the parameters N_H , δ and γ , one can use the fact that $\hat{z}_{OC}^3 + \hat{z}_{OC} + 2\gamma = 0$ (see appendix C). Then, equation (1) reads

$$A_H(\hat{z}_{OC}) = \frac{\delta}{N_H} (1 + \hat{z}_{OC}^2)^{-1}, \quad (3)$$

where \hat{z}_{OC} only depends on γ (see figure 4). We can use this formula to predict the optimum output coupling efficiency for HHG in neon at a peak intensity of $3 \times 10^{14} \text{ W cm}^{-2}$: While γ and thus \hat{z}_{OC} are similar for neon and argon (figure 4), the prefactor $\frac{\delta}{N_H}$ tends to be much smaller in neon, e.g. by a factor of 4 for near-cutoff harmonics (see table B1). Formula (2) predicts output coupling efficiencies around 20% for near-cutoff harmonics in argon. Using the same geometry, optimum output coupling efficiencies up to 50% are expected in neon.

5. Conclusions

In conclusion, we employed a numerical model to reproduce and explain the main features observed in a cavity-enhanced

HHG experiment where the parameters relevant for output coupling and phase matching (backing pressure and gas target position) were systematically scanned. We disentangled the output coupling efficiency from reabsorption, phase matching and the microscopic efficiency with this model, unveiling a trade-off between XUV generation efficiency and output coupling, where the former reaches its optimum values when the gas target is positioned near the focus of the driving beam and the latter favors positions before the focus for the near-cutoff harmonic orders. Reducing the accessible XUV power by up to two orders of magnitude compared to the XUV power produced inside the cavity for the parameters of the studied experiment, we identified this trade-off as an important contribution to the overall conversion efficiency of cavity-based XUV sources with geometric output coupling. We derived an approximate formula for the divergence of the intracavity harmonic beam as a function of gas target position, driving intensity, harmonic order and focusing geometry and explained the physical mechanism behind the observed trade-off. This allowed us to generalize our findings towards HHG with higher photon energies, where a higher optimum output coupling efficiency, but a similar trade-off is expected.

The insights gained in this study provide a quantitative connection between the observable, out-coupled XUV spectrum and the spatial and spectral features of the intracavity macroscopic nonlinear response. On the one hand, together with a thorough understanding of plasma-related limitations, this provides a holistic picture of the different contributions to the overall conversion efficiency and can offer a route towards tapping the full potential of cavity-based XUV sources.

The presented numerical model can be used to investigate alternative geometric output coupling methods, e.g. using quasi-imaging [21, 22] or tailored TEM_{01} modes [20, 31] which promise significantly higher output coupling efficiencies because they permit larger diameters for the output coupling openings thanks to on-axis minima on the mirrors. This may lead to highly efficient cavity-enhanced HHG sources, which will benefit the fields of coincidence spectroscopy, photo-electron spectroscopy/nanoscopy and frequency-comb spectroscopy. On the other hand, the link between the intracavity and the out-coupled XUV can also open up new fields of application, such as HHG spectroscopy at multi-10 MHz repetition rates [32].

Acknowledgments

This research was supported by the Fraunhofer Society/Max-Planck Society cooperation ‘MEGAS’. We are grateful to Nikolai Lilienfein and Johannes Weitenberg for helpful discussions.

Appendix A. Comparison of conversion efficiencies

To compare the record overall conversion efficiencies (driving power P_{in} before enhancement to accessible XUV power

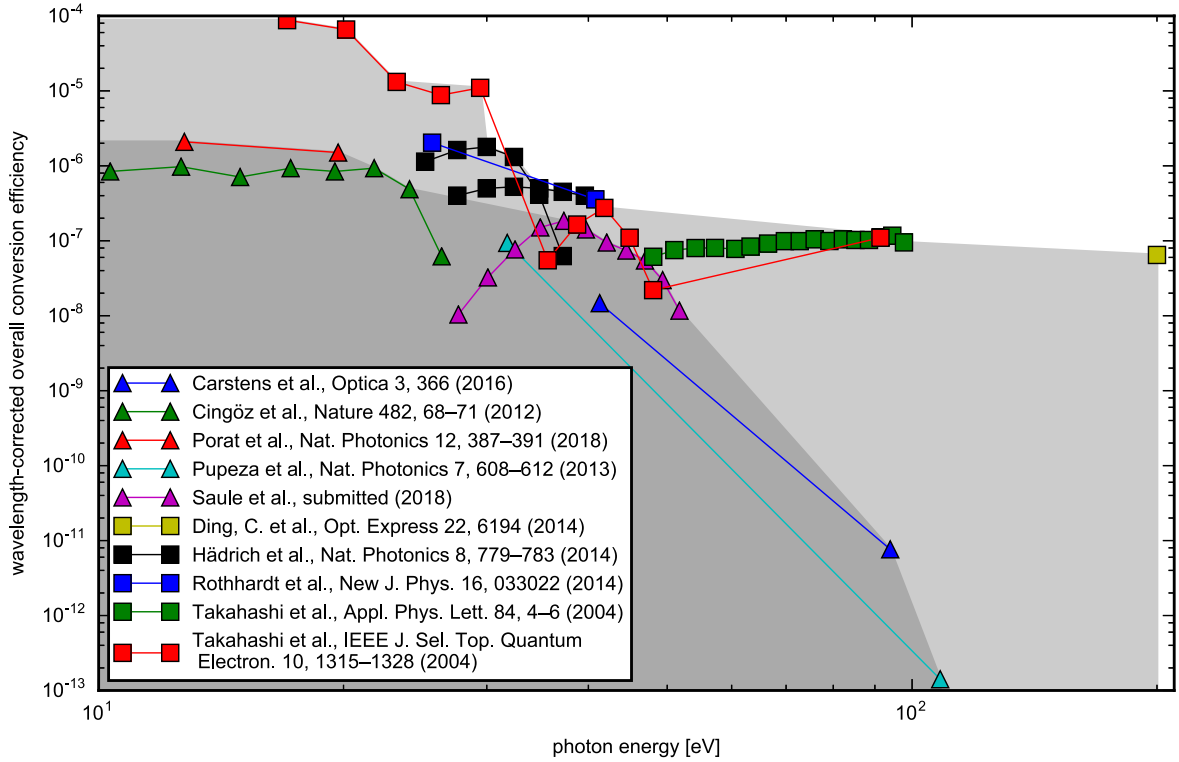


Figure A1. Wavelength-corrected overall conversion efficiencies (driving power before enhancement to accessible XUV power) of cavity-enhanced HHG systems (triangles) and single-pass HHG systems driven by freely propagating Gaussian beams (squares). The shaded areas mark the record conversion efficiencies reached with cavity-based (dark-gray) and single-pass (light-gray) sources.

P_{XUV}) achieved with cavity-based versus single-pass HHG systems, we considered the state-of-the-art sources summarized in [33, figure 3], considering only systems using a freely propagating Gaussian driving beam, and incorporated the results of [16, 17, 34, 35]. To allow for a comparison between systems with different driving wavelengths, we factored out the wavelength scaling of the HHG efficiency with roughly a power of six [36], resulting in a wavelength-corrected conversion efficiency $P_{\text{XUV}}/P_{\text{in}}(\lambda/1030 \text{ nm})^6$.

Figure A1 shows the obtained conversion efficiencies versus the generated photon energies. So far, the overall conversion efficiencies of EC-based sources (dark-gray area) have remained below that of single-pass systems (light-gray area). Keeping in mind that the XUV power generated by HHG in gas targets can scale linearly with the driving power [37], this indicates that inefficiencies in the intracavity XUV generation or the output coupling counteract the typical enhancements of the driving power by several orders of magnitude achieved in ECs.

Appendix B. Analytical model for the single-atom dipole response

For the derivation of the harmonic divergence formula (1) and the generation efficiency formula (D.5), we approximate

the intensity-dependence of the single-atom dipole response $d_H(I)$ for a harmonic order H by a power-law for the absolute value and a linear dependence for the phase (compare e.g. [30]):

$$d_H(I) \propto |I|^{N_H/2} \exp(i\alpha_H I + iH \arg E), \quad (\text{B.1})$$

where $I = \epsilon_0 c/2|E|^2$ is the intensity of the driving field E and N_H and α_H are fitting parameters depending on atomic species, harmonic order, driving field wavelength and on the driving field intensity. We determine α_H for the short trajectory with a Gabor-type analysis as described in [38], providing the intensity-dependent single-atom dipole response computed numerically using a saddle-point approximation [39], which has the advantage of clear separation between trajectories. The exponents N_H were determined by a power-law fit to the intensity-dependent single-atom dipole response in the cutoff region, computed numerically with the Lewenstein formula [27]. The excursion time was limited to 0.66 periods of the driving field to consider only the short trajectory. The resulting parameters for argon and neon are tabulated in table B1, together with the derived quantities $\delta = N_H^2/H^2$ and $\gamma = I\alpha_H/H$, and agree reasonably with the measured values of [30].

Table B1. Parameters used for the analytical model of the single-atom dipole response.

Atom	I (W cm ⁻²)	H	α_H (cm ² W ⁻¹)	N_H	γ	δ	δ/N_H
Ar	1.5×10^{14}	21	-0.3×10^{14}	8.06	-0.02	0.15	0.018
Ar	1.5×10^{14}	23	0.3×10^{14}	8.91	0.02	0.15	0.017
Ar	1.5×10^{14}	25	1.2×10^{14}	9.85	0.07	0.16	0.016
Ar	1.5×10^{14}	27	1.8×10^{14}	10.85	0.10	0.16	0.015
Ar	1.5×10^{14}	29	2.7×10^{14}	11.67	0.14	0.16	0.014
Ar	1.5×10^{14}	31	3.6×10^{14}	12.66	0.17	0.17	0.013
Ar	1.5×10^{14}	33	4.5×10^{14}	13.53	0.20	0.17	0.012
Ar	1.5×10^{14}	35	5.4×10^{14}	14.41	0.23	0.17	0.012
Ar	1.5×10^{14}	37	6.3×10^{14}	15.24	0.25	0.17	0.011
Ar	1.5×10^{14}	39	7.8×10^{14}	16.01	0.30	0.17	0.011
Ar	1.5×10^{14}	41	9.0×10^{14}	16.68	0.33	0.17	0.010
Ar	1.5×10^{14}	43	10.5×10^{14}	16.71	0.36	0.15	0.009
Ne	3.0×10^{14}	35	0.6×10^{14}	13.47	0.05	0.15	0.011
Ne	3.0×10^{14}	37	0.9×10^{14}	14.26	0.07	0.15	0.010
Ne	3.0×10^{14}	39	1.2×10^{14}	15.29	0.09	0.15	0.010
Ne	3.0×10^{14}	41	1.5×10^{14}	16.23	0.11	0.16	0.010
Ne	3.0×10^{14}	43	1.8×10^{14}	17.11	0.13	0.16	0.009
Ne	3.0×10^{14}	45	2.1×10^{14}	18.16	0.14	0.16	0.009
Ne	3.0×10^{14}	47	2.4×10^{14}	19.02	0.15	0.16	0.009
Ne	3.0×10^{14}	49	3.0×10^{14}	19.68	0.18	0.16	0.008
Ne	3.0×10^{14}	51	3.3×10^{14}	20.76	0.19	0.17	0.008
Ne	3.0×10^{14}	53	3.6×10^{14}	20.54	0.20	0.15	0.007
Ne	3.0×10^{14}	55	4.2×10^{14}	20.79	0.23	0.14	0.007
Ne	3.0×10^{14}	57	4.5×10^{14}	20.25	0.24	0.13	0.006
Ne	3.0×10^{14}	59	5.1×10^{14}	19.93	0.26	0.11	0.006
Ne	3.0×10^{14}	61	5.7×10^{14}	20.18	0.28	0.11	0.005
Ne	3.0×10^{14}	63	6.0×10^{14}	19.25	0.28	0.09	0.005
Ne	3.0×10^{14}	65	6.6×10^{14}	19.77	0.30	0.09	0.005
Ne	3.0×10^{14}	67	7.2×10^{14}	19.13	0.32	0.08	0.004
Ne	3.0×10^{14}	69	7.8×10^{14}	18.63	0.34	0.07	0.004
Ne	3.0×10^{14}	71	8.4×10^{14}	18.41	0.35	0.07	0.004
Ne	3.0×10^{14}	73	9.0×10^{14}	18.22	0.37	0.06	0.003
Ne	3.0×10^{14}	75	9.6×10^{14}	16.75	0.38	0.05	0.003
Ne	3.0×10^{14}	77	10.2×10^{14}	17.38	0.40	0.05	0.003
Ne	3.0×10^{14}	79	11.1×10^{14}	16.25	0.42	0.04	0.003

Appendix C. Formula for the XUV divergence

In a similar approach to [30], we approximate the harmonic field as a Gaussian beam by using a Taylor expansion of the radial intensity-dependent phase. In contrast to [30], we do not assume that the gas target is located in the focal plane.

The driving field $E(r)$ at the longitudinal position z of the gas target is given by

$$E(r) \propto \exp\left(-\frac{r^2}{w^2} - ik\frac{r^2}{2R}\right), \quad (\text{C.1})$$

where r is the radial coordinate, $k = 2\pi/\lambda$ the wave number, $w = w_0\sqrt{1 + z^2/z_R^2}$ the beam radius, R the wave-front radius of curvature, w_0 is the beam waist and $z_R = \pi w_0^2/\lambda$ is the Rayleigh range.

In the limit of a small gas target diameter, the harmonic field E_H in the exit plane of the gas target is proportional to the dipole response d_H , which, using (B.1) and (C.1), can be written as

$$\begin{aligned}
E_H(r) &\propto d_H(r) \propto |I|^{N_H/2} \exp(i\alpha_H I(r) + iH \arg E(r)) \\
&\propto |E(r)|^{N_H} \cdot \exp\left(-ikH\frac{r^2}{2R} + i\alpha_H I(r)\right) \\
&= \exp(-r^2/w^2)^{N_H} \cdot \exp\left(-ikH\frac{r^2}{2R} + i\alpha_H I_0 \exp(-2r^2/w^2)\right) \\
&\approx \exp(-N_H r^2/w^2) \cdot \exp\left(-ikH\frac{r^2}{2R} + i\alpha_H I_0(1 - 2r^2/w^2)\right) \\
&\propto \exp(-N_H r^2/w^2) \cdot \exp\left(-ikH\frac{r^2}{2R} - i\alpha_H I_0 2r^2/w^2\right) \\
&= \exp(-N_H r^2/w^2) \cdot \exp\left(-ikH\frac{r^2}{2}\left(\frac{1}{R} + \frac{4\alpha_H I_0}{kHw^2}\right)\right) \\
&= \exp(-r^2/w_H^2) \cdot \exp\left(-\frac{ik_H r^2}{2R_H}\right), \quad (\text{C.2})
\end{aligned}$$

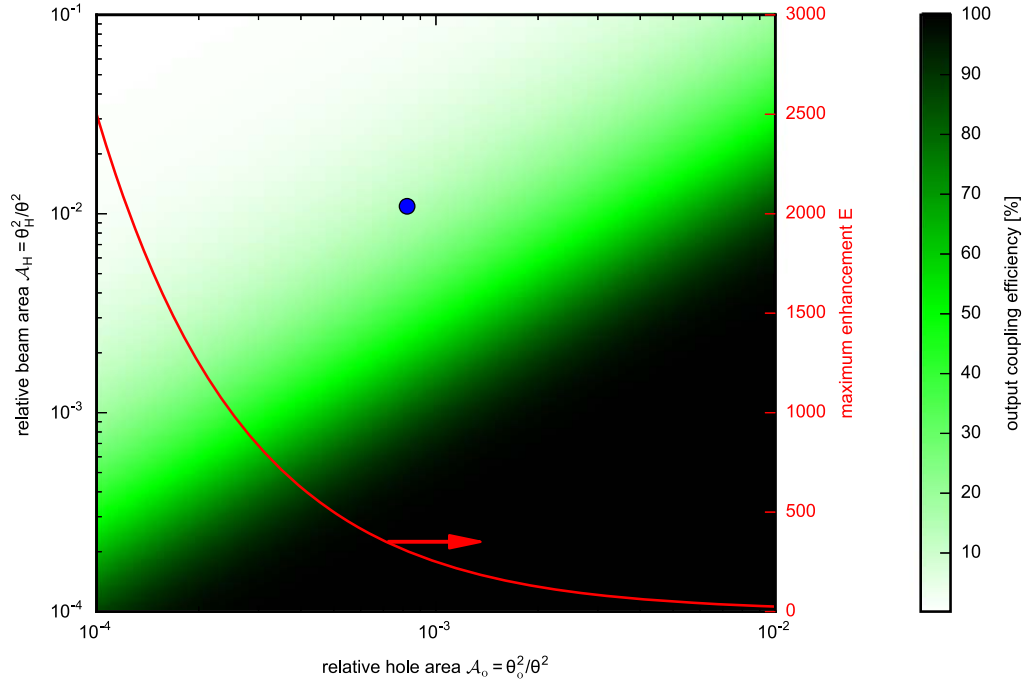


Figure C1. Dependence of the output coupling efficiency (color scale) on the relative hole area \mathcal{A}_o and relative harmonic beam area \mathcal{A}_H . The red line shows the theoretical maximum power enhancements possible for a given relative hole area. The dot marks the parameters of the 33rd harmonic in the simulated experiment.

where we defined the harmonic beam radius

$$w_H := w/\sqrt{N_H}, \quad (\text{C.3})$$

the harmonic radius of curvature

$$R_H := \frac{1}{1/R + 1/R_\phi}, \quad (\text{C.4})$$

the radius of curvature due to the intensity-dependent harmonic phase

$$R_\phi := \frac{k_H w^2}{4\alpha_H I_0}, \quad (\text{C.5})$$

the on-axis intensity

$$I_0 := I(0) = I_f(1 + z^2/z_R^2)^{-1}, \quad (\text{C.6})$$

where I_f is the intensity in the focus and the harmonic wave number

$$k_H := Hk. \quad (\text{C.7})$$

To determine the Rayleigh length $z_{R,H}$ of this Gaussian beam, we use the complex beam parameter q_H :

$$\begin{aligned} z_{R,H} = \Im(q_H) &= \Im\left(\frac{1}{q_H^{-1}}\right) = \Im\left(\frac{1}{R_H^{-1} - i2k_H^{-1}w_H^{-2}}\right) \\ &= \Im\left(\frac{R_H^{-1} + i2k_H^{-1}w_H^{-2}}{R_H^{-2} + 4k_H^{-2}w_H^{-4}}\right) = \frac{2R_H^2 k_H w_H^2}{k_H^2 w_H^4 + 4R_H^2}. \end{aligned} \quad (\text{C.8})$$

The divergence of a harmonic beam can be computed from its Rayleigh length like

$$\theta_H = \sqrt{\frac{2}{k_H z_{R,H}}} = \sqrt{\frac{k_H^2 w_H^4 + 4R_H^2}{R_H^2 k_H^2 w_H^2}} = \sqrt{R_H^2 + \frac{4}{k_H^2 w_H^2}}. \quad (\text{C.9})$$

For a given hole radius r_o and distance Δz between output coupling mirror and focus, one can then compute the fraction of harmonic power transmitted through the hole, i.e. the output coupling efficiency ϵ . Introducing the relative hole area $\mathcal{A}_o := \theta_o^2/\theta^2$, the relative harmonic beam size $\mathcal{A}_H := \theta_H^2/\theta^2$ and the harmonic beam diameter $w_{M,H} := \Delta z\theta_H$ on the output coupling mirror, where $\theta = \sqrt{\frac{2}{kz_R}}$ is the driving beam divergence and $\theta_o := r_o/\Delta z$ is the angle occupied by one hole radius, we can use the well-known formula for the fraction of power of a Gaussian beam transmitted through an aperture:

$$\begin{aligned} \epsilon &= 1 - \exp(-2r_o^2/w_{M,H}^2) = 1 - \exp\left(-2\frac{\theta_o^2 \Delta z^2}{\Delta z^2 \theta_H^2}\right) \\ &= 1 - \exp\left(-2\frac{\theta_o^2}{\theta^2} \frac{\theta^2}{\theta_H^2}\right) = 1 - \exp(-2\mathcal{A}_o/\mathcal{A}_H). \end{aligned} \quad (\text{C.10})$$

Figure C1 shows the dependence of the output coupling efficiency ϵ on \mathcal{A}_o and \mathcal{A}_H . Using a computer algebra system

to substitute the expressions defined above, it can be verified that

$$\mathcal{A}_H = \frac{1}{N_H} \frac{(\hat{z}^3 + \hat{z} + 2\gamma)^2 + (1 + \hat{z}^2)^2 \delta}{(1 + \hat{z}^2)^3}, \quad (\text{C.11})$$

where $\hat{z} = z/z_R$ is the scaled gas target position and $\gamma := \alpha_H I_f / H$ and $\delta := N_H^2 / H^2$. The term $\hat{z}^3 + \hat{z} + 2\gamma$ has exactly one real root \hat{z}_{OC} because its derivative is positive everywhere, and this root corresponds to the target positions for which $1/R_H$ vanishes (this is also easily verified by using a computer algebra system).

We numerically determined the minima of $\mathcal{A}_H(\hat{z})$ for values of γ from -1 to 1 and values of δ in the range tabulated in table B1 and found that the minima deviate by less than 0.04 from \hat{z}_{OC} . Consequently, the position of the minimum has no strong dependence on δ and \hat{z}_{OC} can be regarded as an excellent approximation for the optimum gas target position for output coupling.

Figure 4 shows the dependence of \hat{z}_{OC} on γ . The corridor marks the region over which \mathcal{A}_H deviates by less than a factor of 2 from the optimum value, assuming $\delta = 0.17$ (value for 33rd harmonic in argon). The diameter of the corridor increases with δ and remains between 0.20 and 1.0 for the tabulated values of δ .

Appendix D. Formula for the XUV power

Neglecting the plasma and Kerr phase, the on-axis phase of the driving Gaussian beam is

$$\phi_1(z) = -nkz + \underbrace{\arctan(z/z_R)}_{\text{Gouy phase}}, \quad (\text{D.1})$$

where n is the refractive index at the driving wavelength. Approximating the intensity-dependent harmonic dipole phase $\phi(I)$ by a linear dependence (see appendix B), the total harmonic dipole phase is then

$$\phi_H(z) = H\phi_1(z) + \underbrace{\alpha_H I(z)}_{\text{intensity-dependent phase}} + C. \quad (\text{D.2})$$

This yields an effective wave number of

$$\begin{aligned} k_{\text{eff}} &= -\partial_z \phi_H(z) = -H\partial_z \phi_1(z) - \alpha_H \partial_z I(z) \\ &= -H(-nk + \partial_z \arctan(z/z_R)) \\ &\quad - \alpha_H I_f \partial_z (1 + z^2/z_R^2)^{-1} \\ &= nkH - H \frac{1/z_R}{1 + z^2/z_R^2} + \alpha_H I_f (1 + z^2/z_R^2)^{-2} 2z/z_R^2, \end{aligned} \quad (\text{D.3})$$

where I_f is the peak intensity in the focus. Good phase matching is reached for $k_{\text{eff}} \approx n_H kH$, where H is the harmonic order and n_H is the refractive index at the

corresponding wavelength. $\Delta k_H = k_{\text{eff}} - n_H kH$ quantifies the phase mismatch and should vanish:

$$\begin{aligned} \Delta k_H &= Hk(n - n_H) - H \frac{1/z_R}{1 + z^2/z_R^2} \\ &\quad + \alpha_H I_f (1 + z^2/z_R^2)^{-2} 2z/z_R^2 \stackrel{!}{=} 0 \\ \Leftrightarrow Hk \Delta n_{\text{std}} \frac{\rho}{\rho_{\text{std}}} &= H \frac{1/z_R}{1 + z^2/z_R^2} \\ &\quad - \alpha_H I_f (1 + z^2/z_R^2)^{-2} 2z/z_R^2 \\ \Rightarrow \rho &\propto \frac{1}{1 + \hat{z}^2} - 2\gamma \frac{\hat{z}}{(1 + \hat{z}^2)^2}. \end{aligned} \quad (\text{D.4})$$

Here, we defined $\hat{z} := z/z_R$ and $\gamma := \frac{\alpha_H I_f}{H}$ (compare appendix C) and used $n - n_H = \frac{\rho}{\rho_{\text{std}}} \Delta n_{\text{std}}$, where ρ is the density in the gas target, ρ_{std} is the density at standard conditions and Δn_{std} the refractive index difference at standard conditions.

To estimate the harmonic power P_H generated in a harmonic order H at a certain position of the nozzle, we assume generation at the phase-matching density as given by (D.4) and that the amplitude E_H of the emitted harmonic field is proportional to the number of emitters (density \times mode size). The intensity-dependence of the single-atom dipole response is approximated by a power law (see appendix B), yielding

$$\begin{aligned} P_H &\propto E_H^2 \propto (\rho w^2 I^{N_H/2})^2 \propto (\rho(1 + \hat{z}^2)(1 + \hat{z}^2)^{-N_H/2})^2 \\ &= \rho^2 (1 + \hat{z}^2)^{2-N_H}. \end{aligned} \quad (\text{D.5})$$

Using (D.5) and (D.4), we can estimate the generated harmonic power for a given gas target position \hat{z} and parameters γ and N_H . This allows us to numerically compute the target position for optimum power and the corridor over which P_H deviates by less than a factor of 2 from the optimum value (figure 4, for $N_H = 13.53$).

The optimum value \hat{z}_{gen} remains close to zero, deviating by less than 0.18 for values of γ from -1 to 1 and values of N_H in the range tabulated in table B1. The diameter of the corridor decreases slightly with N_H and remains between 0.34 and 0.60 .

ORCID iDs

M Högner  <https://orcid.org/0000-0002-6243-802X>
I Pupeza  <https://orcid.org/0000-0001-8422-667X>

References

- [1] McPherson A, Gibson G, Jara H, Johann U, Luk T S, McIntyre I A, Boyer K and Rhodes C K 1987 Studies of multiphoton production of vacuum-ultraviolet radiation in the rare gases *J. Opt. Soc. Am. B* **4** 595–601
- [2] Ferray M, L’Huillier A, Li X F, Lompre L A, Mainfray G and Manus C 1988 Multiple-harmonic conversion of 1064 nm

- radiation in rare gases *J. Phys. B: At. Mol. Opt. Phys.* **21** L31–5
- [3] Krausz F and Ivanov M 2009 Attosecond physics *Rev. Mod. Phys.* **81** 163–234
- [4] Krausz F and Stockman M I 2014 Attosecond metrology: from electron capture to future signal processing *Nat. Photon.* **8** 205–13
- [5] Constant E, Garzella D, Breger P, Mével E, Dorrer C, Le Blanc C, Salin F and Agostini P 1999 Optimizing high harmonic generation in absorbing gases: model and experiment *Phys. Rev. Lett.* **82** 1668–71
- [6] Rothhardt J *et al* 2014 53W average power few-cycle fiber laser system generating soft x rays up to the water window *Opt. Lett.* **39** 5224
- [7] Rothhardt J *et al* 2016 High-repetition-rate and high-photon-flux 70 eV high-harmonic source for coincidence ion imaging of gas-phase molecules *Opt. Express* **24** 18133
- [8] Lorek E, Larsen E W, Heyl C M, Carlström S, Paleček D, Zigmantas D and Mauritsson J 2014 High-order harmonic generation using a high-repetition-rate turnkey laser *Rev. Sci. Instrum.* **85** 123106
- [9] Hädrich S, Klenke A, Rothhardt J, Krebs M, Hoffmann A, Pronin O, Pervak V, Limpert J and Tünnermann A 2014 High photon flux table-top coherent extreme-ultraviolet source *Nat. Photon.* **8** 779–83
- [10] Chiang C-T, Huth M, Trützscher A, Kiel M, Schumann F O, Kirschner J and Widdra W 2015 Boosting laboratory photoelectron spectroscopy by megahertz high-order harmonics *New J. Phys.* **17** 013035
- [11] Mills A K, Zhdanovich S, Sheyerman A, Levy G, Damascelli A and Jones D J 2015 An XUV source using a femtosecond enhancement cavity for photoemission spectroscopy *Advances in X-ray Free-Electron Lasers Instrumentation III 95121* *SPIE Optics + Optoelectronics (Proc. SPIE 9512)*
- [12] Corder C, Zhao P, Bakalis J, Li X, Kershish M D, Muraca A R, White M G and Allison T K 2018 Ultrafast extreme ultraviolet photoemission without space charge *Struct. Dyn.* **5** 054301
- [13] Ozawa A and Kobayashi Y 2013 Vuv frequency-comb spectroscopy of atomic xenon *Phys. Rev. A* **87** 022507
- [14] Cingöz A, Yost D C, Allison T K, Ruehl A, Fermann M E, Hartl I and Ye J 2012 Direct frequency comb spectroscopy in the extreme ultraviolet *Nature* **482** 68–71
- [15] Pupeza I *et al* 2013 Compact high-repetition-rate source of coherent 100 eV radiation *Nat. Photon.* **7** 608–12
- [16] Carstens H *et al* 2016 High-harmonic generation at 250 MHz with photon energies exceeding 100 eV *Optica* **3** 366
- [17] Saule T *et al* 2019 High-flux ultrafast extreme-ultraviolet photoemission spectroscopy at 18.4 MHz pulse repetition rate *Nat. Commun.* **10** 458
- [18] Porat G, Heyl C M, Schoun S B, Benko C, Dörre N, Corwin K L and Ye J 2018 Phase-matched extreme-ultraviolet frequency-comb generation *Nat. Photon.* **12** 387–91
- [19] Saule T, Högner M, Lilienfein N, de Vries O, Plötner M, Yakovlev V S, Karpowicz N, Limpert J and Pupeza I 2018 Cumulative plasma effects in cavity-enhanced high-order harmonic generation in gases *APL Photonics* **3** 101301
- [20] Moll K D, Jones R J and Ye J 2006 Output coupling methods for cavity-based high-harmonic generation *Opt. Express* **14** 8189
- [21] Pupeza I *et al* 2014 Cavity-enhanced high-harmonic generation with spatially tailored driving fields *Phys. Rev. Lett.* **112** 103902
- [22] Weitenberg J, Rußbüldt P, Pupeza I, Udem T, Hoffmann H-D and Poprawe R 2015 Geometrical on-axis access to high-finesse resonators by quasi-imaging: a theoretical description *J. Opt.* **17** 025609
- [23] Allison T K, Cingöz A, Yost D C and Ye J 2011 Extreme nonlinear optics in a femtosecond enhancement cavity *Phys. Rev. Lett.* **107** 183903
- [24] Holzberger S *et al* 2015 Femtosecond enhancement cavities in the nonlinear regime *Phys. Rev. Lett.* **115** 023902
- [25] Högner M, Tosa V and Pupeza I 2017 Generation of isolated attosecond pulses with enhancement cavities—a theoretical study *New J. Phys.* **19** 033040
- [26] Geissler M, Tempea G, Scrinzi A, Schnürer M, Krausz F and Brabec T 1999 Light propagation in field-ionizing media: extreme nonlinear optics *Phys. Rev. Lett.* **83** 2930
- [27] Lewenstein M, Balcou P, Ivanov M Y, L’huillier A and Corkum P B 1994 Theory of high-harmonic generation by low-frequency laser fields *Phys. Rev. A* **49** 2117
- [28] Scoles G 1988 *Atomic and Molecular Beam Methods* vol 1 (Oxford: Oxford University Press)
- [29] Voelz D G 2011 *Computational Fourier Optics—A MATLAB® Tutorial (Tutorial Texts in Optical Engineering vol 89)* (Bellingham, WA: SPIE) (<https://doi.org/10.1117/3.858456>)
- [30] Carlström S *et al* 2016 Spatially and spectrally resolved quantum path interference with chirped driving pulses *New J. Phys.* **18** 123032
- [31] Högner M, Saule T, Lilienfein N, Pervak V and Pupeza I 2018 Tailoring the transverse mode of a high-finesse optical resonator with stepped mirrors *J. Opt.* **20** 024003
- [32] Marangos J P 2016 Development of high harmonic generation spectroscopy of organic molecules and biomolecules *J. Phys. B: At. Mol. Opt. Phys.* **49** 132001
- [33] Rothhardt J, Tadesse G K, Eschen W and Limpert J 2018 Table-top nanoscale coherent imaging with XUV light *J. Opt.* **20** 113001
- [34] Rothhardt J, Krebs M, Hädrich S, Demmler S, Limpert J and Tünnermann A 2014 Absorption-limited and phase-matched high harmonic generation in the tight focusing regime *New J. Phys.* **16** 033022
- [35] Takahashi E J, Nabekawa Y and Midorikawa K 2004 Low-divergence coherent soft x-ray source at 13 nm by high-order harmonics *Appl. Phys. Lett.* **84** 4–6
- [36] Shiner A D *et al* 2009 Wavelength scaling of high harmonic generation efficiency *Phys. Rev. Lett.* **103** 073902
- [37] Heyl C M *et al* 2016 Scale-invariant nonlinear optics in gases *Optica* **3** 75
- [38] Balcou P, Dederichs A S, Gaarde M B and L’Huillier A 1999 Quantum-path analysis and phase matching of high-order harmonic generation and high-order frequency mixing processes in strong laser fields *J. Phys. B: At. Mol. Opt. Phys.* **32** 2973
- [39] Ivanov M Y, Brabec T and Burnett N 1996 Coulomb corrections and polarization effects in high-intensity high-harmonic emission *Phys. Rev. A* **54** 742–5